Plasma Science and
Technology

ACCEPTED MANUSCRIPT

Optimization of Electron Beams for Ion Bombardment Secondary Emission Electron Gun

To cite this article before publication: Zebin Wang *et al* 2024 *Plasma Sci. Technol.* in press https://doi.org/10.1088/2058-6272/ad9819

Optimization of electron beams for ion bombardment secondary emission electron gun

Zebin WANG (王泽彬)[1,2], Junbiao LIU (刘俊标)[1,2,*], Aiguo CHEN (陈爱国)[3,*], Dazheng WANG (王大正)[1], Pengfei WANG (王鹏飞)[1], and Li HAN (韩立)[1,2]

[1]Institute of Electrical Engineering, Chinese Academy of Sciences, Beijing 100190, People's Republic of China

[2]University of Chinese Academy of Sciences, Beijing 100049, People's Republic of China

[3]Hypervelocity Aerodynamics Institute, China Aerodynamics Research and Development Center, Mianyang 621000, People's Republic of China

[*]E-mail of corresponding author: liujb@mail.iee.ac.cn

Abstract

Electron beam fluorescence technology is an advanced non-contact measurement in rarefied flow fields, and the fluorescence signal intensity is positively correlated with the electron beam current. The ion bombardment secondary emission electron gun is suitable for the technology. To enhance the beam current, COMSOL simulations and analyses were conducted to examine plasma density distribution in the discharge chamber under the effects of various conditions and the electric field distribution between the cathode and the spacer gap. The anode shape and discharge pressure conditions were optimized to increase plasma density. Additionally, an improved spacer structure was designed with the dual purpose of enhancing the electric field distribution between the cathode-spacer gaps and improving vacuum differential effects. This design modification aims to increase the pass rate of secondary electrons. Both simulation and experimental results demonstrated that the performance of the optimized electron gun was effectively enhanced. When the electrode voltage remains constant and the discharge gas pressure is adjusted to around 8 Pa, the maximum beam current was increased from 0.9 mA to 1.6 mA.

Keywords: air plasma, secondary emission electron gun, electron beam, performance optimization

(Some figures may appear in colour only in the online journal)

1 . Introduction

Electron beam fluorescence (EBF) technology is an advanced non-contact method for measuring parameters in hypersonic flow fields. Its principle is based on the interaction between gas molecules and high-energy electrons under rarefied conditions, where ground-state gas molecules are excited and emit fluorescence as they return to a stable ionic ground state. The flow field can be displayed by fluorescence. Additionally, the rotational temperature can be obtained by analyzing the rotational spectral

lines in the fluorescence, while the vibrational temperature can be derived from the vibrational bands. Furthermore, the density can be resolved through the fluorescence intensity, and the velocity can be determined by the pulsed electron beam fluorescence [1]. Compared with traditional measurement techniques such as Pitot tubes [2], Particle Image Velocimetry (PIV) [3] and Interferometric Rayleigh Scattering (IRS) [4], EBF technology has the advantages of not contaminating or disturbing the flow field and enabling multi-point measurements within the boundary layer [5], making it suitable for hypersonic flow field parameter measurements [6]. As the core component of EBF technology, the secondary emission electron gun (SEEG), based on the principle of secondary electron emission, offers advantages over traditional thermionic and field emission electron guns [7] in terms of compact structure, suitability for low-pressure environments in rarefied flow field [8] and longer performance life [9], meeting the requirements for lightweight electron gun equipment for rarefied flow field parameter testing. According to the principles of EBF technology, the intensity of the fluorescence signal is related to the electron beam current that excites the gas molecules in the rarefied flow field [10]. The improvement of the signal-to-noise ratio, and consequently the enhancement of measurement accuracy, can be facilitated by a stronger fluorescence signal. Therefore, increasing the beam current of the secondary emission electron gun has become one of the key areas of focus in its performance optimization.

In 1995, Cherenshchikov *et al* [11] proposed a secondary emission magnetron gun, which utilizes crossed fields to accelerate the spiral motion of electrons in the discharge region and continuously bombard the copper cathode to generate secondary electrons, and these electrons are eventually extracted to achieve a high-current electron beam. To further enhance the beam current, they also investigated the secondary electron emission coefficients of electrodes made from different

materials. However, it is unsuitable for directly application in EBF technology because the gun requires operation at several hundred kilovolts and produces a beam with annular cross-section. In 2002, Chalise *et al* [12] developed a SEEG for the treatment of nitrous oxide gases. To achieve higher beam current, they used a wire ion plasma source (WIPS) to generate ions, which were accelerated by a grid to bombard a cathode plate and to form a large-area electron beam. However, the required accelerating voltage is 100 kV and the energy density of the electron beam is relatively low. In 2014, Kui *et al* [13] designed a micro-pulsed SEEG, which is based on the principle of secondary electron multiplication. By applying a radio-frequency electric field between discharge plates, electrons continuously oscillated at high frequency between the plates, gaining energy and exciting the gas between the plates to generate more secondary electrons, thereby increasing the electron beam current. However, due to the high vacuum requirements of the electron gun (10^{-5} Pa), there is a significant difference compared to the low-pressure working environment (100 Pa) required for hypersonic rarefied flow field testing, which are the challenges for the construction of the EBF testing system. In summary, over the past decades, researchers have attempted to increase the beam current of SEEGs by using metal electrode materials with higher secondary electron emission coefficients and introducing higher discharge voltages. Nonetheless, to meet the requirements of EBF testing, the critical challenge remains how to reduce the power consumption and vacuum requirements of the SEEG while increasing its beam current. In 2022, the Institution of Electrical Engineering Chinese Academy of Science (IEECAS) completed the development of a model and experimental platform for an ion bombardment SEEG. To meet the requirements for EBF testing, further optimization research is needed for the beam current of the ion bombardment SEEG.

The emission performance of an ion bombardment SEEG based on gas discharge theory and vacuum simulation theory was analyzed in this study. COMSOL Multiphysics software simulations were conducted to study the impact of parameters such as plasma density and spacer structure size on the beam current of existing electron guns. Verification experiments were designed to determine the feasibility of the optimization schemes, providing a reference for the structural design of ion bombardment SEEGs with higher beam current.

2 Optimization simulation principle of electron gun

2.1 Structure and principle of electron gun

The structure of the ion bombardment SEEG is shown in figure 1. The positive high voltage is connected to the discharge anode (R_1 = 100 kΩ), which undergoes DC glow discharge in the lower discharge chamber (R_2 = 2 MΩ), with plasma being generated in a low vacuum environment (5–10 Pa). Positive ions in the plasma are accelerated and migrate upward into the upper accelerating chamber due to the combined effects of the cathode electric field and the pressure differential between the two chambers. The cathode of the SEEG is made of aluminum, a metal with a high secondary electron emission coefficient[14], which readily forms a dense layer of aluminum oxide in air (with an even higher coefficient), effectively resisting ion bombardment and thus extending its service life. The discharge anode is annular and made of tungsten, while the rodlike anode is made of stainless steel. These electrons are then accelerated in the opposite direction to produce the desired electron beam. This electron beam is further accelerated by the electric field between the negatively charged cathode and the spacer aperture, passing through the spacer aperture, discharge chamber, the focusing magnetic lens and the pressure differential tube. A high-energy electron beam is ultimately formed.

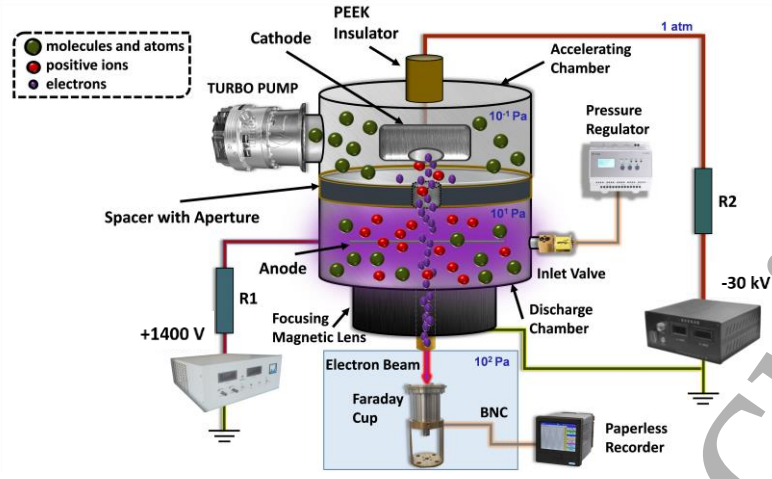

Figure 1. Schematic of ion bombardment secondary emission electron gun.

The factors influencing the beam current of the ion bombardment SEEG are mainly:

(1) Ion quantity. In terms of electron beam generation process, the factors influencing secondary electron yield [15] include the material of the solid surface, the angle of incidence, ion energy, and ion quantity [16]. With the cathode potential and the structure of the electron gun remaining unchanged, the secondary electron yield is primarily influenced by the quantity of ions bombarding the cathode. The plasma generated by the low-pressure DC glow discharge in the discharge chamber (in figure 1) serves as the ion source. Near the central axis of the discharge chamber, ions are accelerated and migrate upward due to the combined effects of the cathode electric field and the pressure differential induced by the spacer. Therefore, the plasma density at the axis position indirectly affects the final beam current intensity of the electron gun.

(2) The shape of the spacer. In the electron beam transmission process, secondary electrons are constrained by the electric field distribution between the cathode and anode, accelerating and passing through the apertures of the spacer. The shape and size of the spacer directly affect the final beam current of the electron gun.

Based on the above analysis, the main factors influencing the beam current of electron gun are low plasma density near the central axis of the discharge chamber, and secondary electrons' ability to efficiently pass through the spacer aperture.

2.2 Principle of plasma simulation

Plasma simulation based on COMSOL uses the fluid model [17] to compute the gas discharge process. The state of direct current discharge plasma can be described by the drift-diffusion module, the heavy particle transport module [18], and the electrostatic module, which are all coupled within COMSOL [19].

The drift-diffusion module [20] is primarily described by the electron continuity equation and the electron energy conservation equation:

$$\begin{cases} \frac{\partial}{\partial t}(n_e) + \nabla \cdot \boldsymbol{\Gamma}_e = R_e \\ \frac{\partial}{\partial t}(n_\varepsilon) + \nabla \cdot \boldsymbol{\Gamma}_\varepsilon + \boldsymbol{E} \cdot \boldsymbol{\Gamma}_e = S_{en} \end{cases} \quad (1)$$

In the formula, n_e represents the electron density, n_ε represents the electron energy, R_e represents the electron source term, characterizing the change in electron density caused by inelastic collisions. S_{en} represents the loss of electron energy due to inelastic collisions. $\boldsymbol{\Gamma}_e$ represents the electron flux vector, expressed as:

$$\boldsymbol{\Gamma}_e = n_e \boldsymbol{u}_e = -(\mu_e \cdot \boldsymbol{E}) n_e - \nabla(D_e n_e). \quad (2)$$

In the equation, $\boldsymbol{u}_e$ represents the electron drift velocity. μ_e is the electron mobility, and D_e is the electron diffusion coefficient. The first term on the right side of the equation represents the drift flux, and the second term represents the diffusion flux. The electron continuity equation indicates that the change in electron density is equal to the change in density caused by electron drift and diffusion, plus the change caused by electron source terms due to inelastic collisions, etc.

$\boldsymbol{\Gamma}_\varepsilon$ represents the electron energy flux vector, expressed as:

$$\boldsymbol{\Gamma}_\varepsilon = -(\mu_\varepsilon \cdot \boldsymbol{E})n_\varepsilon - \nabla(D_\varepsilon n_\varepsilon). \quad (3)$$

In the plasma simulation, the initial number of electrons is set to $n_0 = 10^{10}$ m^{-3}, and the initial average energy of the electrons is set to 4 eV. The set of equations indicates that the change in electron number density n_e and energy equals the sum of changes due to electron drift diffusion and external electric field, plus changes in electron source terms due to inelastic collisions, among other factors .

The heavy species transport module is primarily described by the heavy particle mass conservation equation:

$$\rho \cdot \frac{\partial}{\partial t}(\omega_k) + \rho(\boldsymbol{u} \cdot \nabla)\omega_k = \nabla \cdot j_k + R_k. \quad (4)$$

In the equation, j_k represents the diffusion flux vector, R_k denotes the reaction rate of the k-th species (in kg/(m³·s)), $\boldsymbol{u}$ is the mass-averaged velocity vector (in m/s), ρ indicates the density of the mixture (in kg/m³), and ω_k represents the mass fraction of the k-th species. The "mixture-averaged model" is chosen for the diffusion model in the heavy ion transport module for higher accuracy [21] . The advantage of the mixture-averaged model is that it fully satisfies mass conservation. It has significantly lower computational costs than solving the full Maxwell-Stefan equations (which cannot be used in the heavy particle transport module) [22]. The electrostatic module is mainly described by the Poisson equation:

$$-\nabla \cdot (\varepsilon_0 \varepsilon_r \nabla V) = \rho_q. \quad (5)$$

In the equation, V is the potential, ε_0 is the vacuum dielectric constant, ε_r is the relative dielectric constant, and ρ_q is the space charge density. The Poisson equation describes the distribution of electric potential, and by combining it with the definition of electric potential, the electric field distribution in the discharge chamber can be calculated.

2.3 Calculation of conductance through spacer aperture

As shown in figure 1, the accelerating chamber and the discharge chamber are divided by a spacer aperture, with the pressure difference between the two chambers maintained by the gas resistance of the central aperture in the spacer. The diameter of the aperture can be increased to improve the secondary electron transmission rate, but the pressure in the accelerating chamber will also be raised, potentially causing cathode arcing and breakdown. Therefore, the length of the aperture needs to be increased to stabilize the pressure difference, but the risk of breakdown between the cathode and the spacer gap may also be increased. Hence, it is crucial for a reasonable spacer structure to be designed to balance conductance and electric field requirements. The two vacuum chambers are connected by a pipeline that can be simplified as a cylindrical straight pipe. According to the principle of vacuum pipeline conductance, the conductance of the pipe is related to the state of gas flow, the pumping speed of the vacuum pump, and the pressure difference between the two chambers, which can be expressed as:

$$p_1 - p_2 = \frac{Q}{C}. \quad (6)$$

In the equation, p_1 and p_2 represent the pressures at the high-pressure and low-pressure ends of the pipeline (in Pa). Q is the gas flow rate through the pipeline, which is the product of the pumping speed and pressure, expressed as: $Q = S \cdot P$ (in Pa·L/s). The gas flow rate characterizes the amount

of gas passing through a given cross-section per unit time and is related to the pumping speed of the vacuum pump. C represents the gas conductance, which is a constant related to the state of gas flow, the geometric parameters of the duct (or aperture), gas temperature, and the type of gas (in L/s). Using the Knudsen criterion [23], the gas flow state in the pipeline is identified as viscous-molecular flow. Substituting pipeline length (L) = 5 mm, the conductance of the planar aperture spacer is calculated to be C = 5.55 L/s.

The spacer aperture structure is optimized to ensure the pressure difference between the two chambers of the electron gun while the aperture diameter is expanded. In this way, a sufficiently low pressure in the accelerating chamber is maintained to prevent breakdown and sparking between the cathode and the spacer gap. As shown in figure 2, the actual dimensions and machining precision of the accelerating chamber are considered, the spacer structure with an aperture of D = 8 mm and L = 12 mm was chosen, so that the flow conductance can be reduced to 4.29 L/s. The reduction in conductance helps to prevent discharge phenomena in the accelerating chamber where the cathode is located.

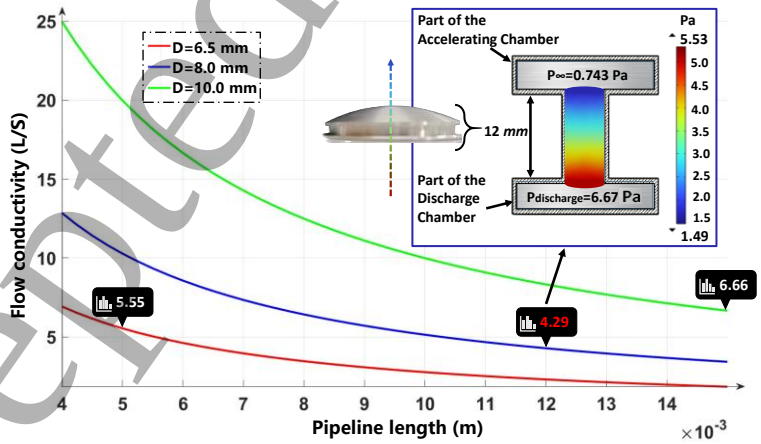

Figure 2. The relationship between the length of the tube and air resistance at different sections.

In summary, the optimization method for the beam current of the ion bombardment S EEG in this paper includes: enhancing the plasma density near the central axis of the disc harge chamber by altering the discharge anode shape and discharge pressure conditions thr ough plasma simulation; and improving the secondary electron transmission rate by optimiz ing the spacer structure and electric field distribution through vacuum simulation, conducta nce calculations, electric field and particle simulations.

3 Optimization simulation

3.1 The impact of discharge chamber pressure on plasma density

According to Paschen's law [24], with the chamber inner diameter of 70 mm and the actual discharge pressure in the range of 5–10 Pa, the higher the discharge pressure in the chamber, the lower the breakdown voltage, which makes the occurrence of the DC glow discharge facilitated. Therefore, the breakdown voltage can be lowered and the cost of the DC excitation source can be reduced by increasing the discharge chamber pressure.

On the other hand, the discharge pressure in the chamber affects the plasma density of the gas discharge, as shown in figure 3: at lower pressures, the distance between gas molecules is greater, which is reduced in the collision probability between electrons and gas molecule. Simultaneously, with the increment of the mean free path of electrons, the ionization efficiency per collision is enhanced, which makes electrons gain more energy on average. As the pressure increases, the density of gas molecules is increased, which results in more frequent collisions between electrons and gas molecules. This increase in collisions leads to an increased ionization probability and aids in plasma formation. However, if the pressure continues to rise, electrons will lose kinetic energy more quickly

due to frequent collisions with the dense gas molecules, which reduces the electron energy and affects ionization efficiency.

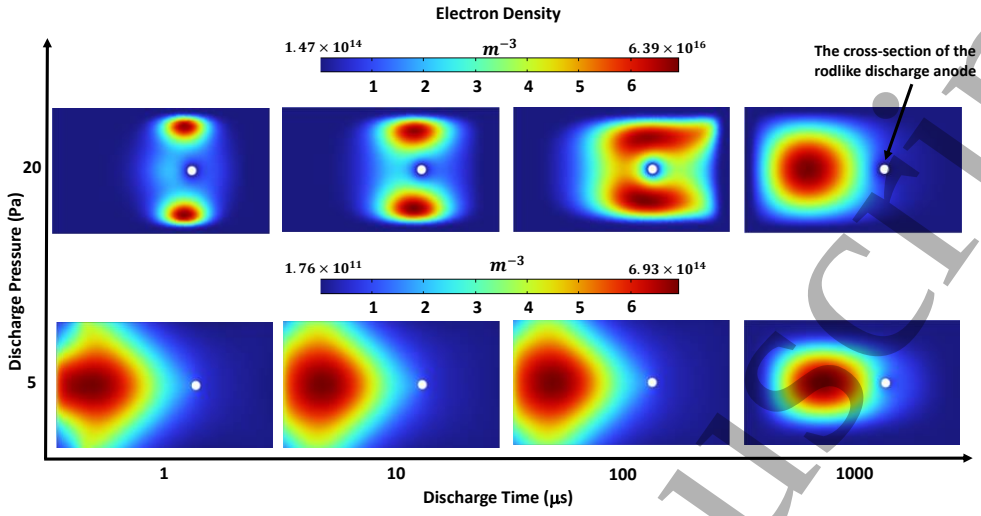

Figure 3. Comparison of plasma establishment process under different pressures (longitudinal cross-sectional view).

The simulation results of the plasma density establishment process under different pressures, as well as the spatial distribution of the glow, are illustrated in figures 4 and 5. The results indicate that when the discharge pressure is in the range of 5–8.5 Pa, the number of particles participating in plasma chemical reactions is increased. Consequently, the plasma density within the discharge chamber increases with the rise in pressure. Additionally, the maximum plasma density is observed at the center of the discharge chamber, with a uniform distribution in the vertical direction. The simulation results of plasma density are consistent with the experimental observations.

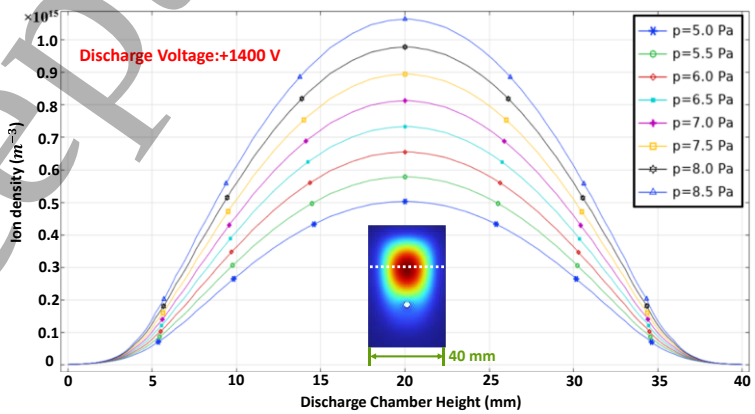

Figure 4. Comparison of ion density simulation results under different pressure along the chamber's height.

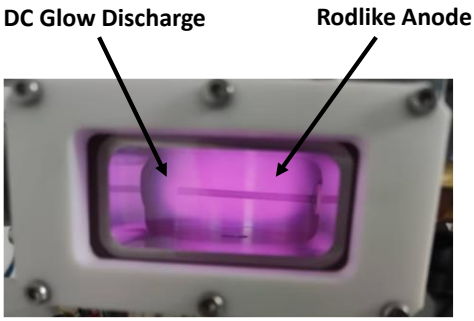

Figure 5. Side view of the spatial distribution of glow discharge.

3.2 The impact of discharge anode geometry on plasma density

In gas discharge processes, the shape of the anode determines the spatial distribution and density of the DC glow discharge plasma. Different anode shapes lead to varying electric field distributions, thereby affecting plasma formation and maintenance. In the simulations, the discharge chamber pressure is set to 6 Pa, with an anode voltage of 1400 V. The discharge chamber features a rod-shaped anode, offset 10 mm from the central axis, with a diameter of 3 mm, made of stainless steel, and a thin ring-shaped electrode encircling the central axis, with a diameter of 0.2 mm, made of tungsten. The simulation results of plasma density are shown in figures 6 and 7.

The results indicate that the curvature radius is decreased when the rod-shaped electrode is replaced with a ring-shaped tungsten wire electrode. A more significant charge accumulation effect is brought about near the electrode, which in turn enhances the local field strength. During the initial discharge phase, more kinetic energy is gained by electrons near the anode, which facilitates gas discharge and the plasma density within the discharge chamber can be increased. Additionally, a more uniform overall spatial distribution of plasma is achieved by the thin ring-shaped tungsten electrode compared to the rod-shaped electrode. The maximum particle density appears near the axis. As the plasma serves as the ion source for ion bombardment of the cathode, under the discharge of the thin ring-shaped electrode, more ions will pass through the upper spacer aperture and are

accelerated toward the cathode. This process yields more secondary electrons, ultimately the beam current of the electron gun is enhanced.

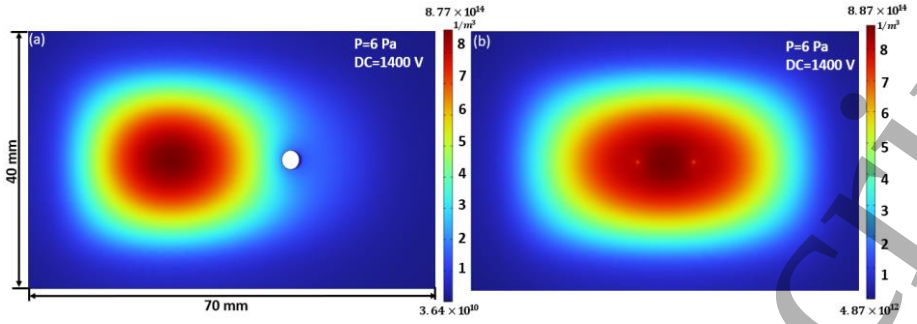

Figure 6. Comparison of plasma density simulation results. (a) Rod electrode, (b) ring electrode.

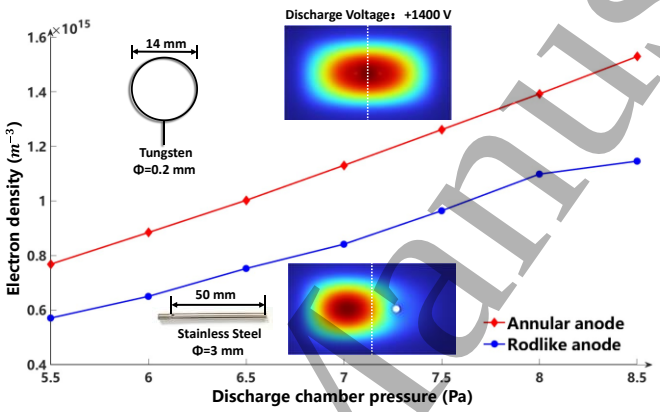

Figure 7. Comparison of plasma density at axis position of different anodes under different pressure.

3.3 The Simulation of cathodic-spacer gap electric field and particle

The cathode is connected to −30 kV DC high voltage. The potential distribution between the cathode and the spacer gap under two different spacer structures is shown in figure 8. Under the curved spacer structure (curvature radius: 125 mm), the curvature of the potential line near the aperture region is reduced, which results in an electric field that is more converged. The acceleration of secondary electrons through the spacer aperture is facilitated by this configuration under the influence of the electric field, which leads to the formation of an electron beam.

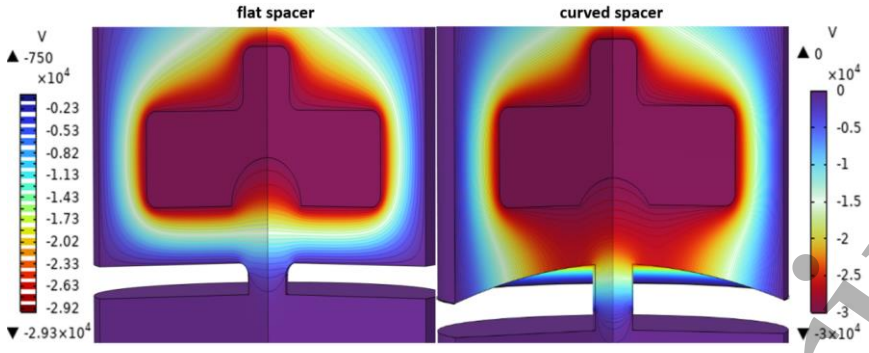

Figure 8. Comparison of electric field structures under two types of spacer structures.

The electron trajectories under the two spacer structures are shown in figure 9. The electronic trajectory is calculated through the electrostatic field module and charged particle tracking module in COMSOL. The particle simulation results indicate that the curved spacer experiences higher gas resistance and higher cathode partial pressure. Consequently, secondary electrons not only converge under the electric field force but also gain more energy. As a result, the energy of the final electron beam is increased.

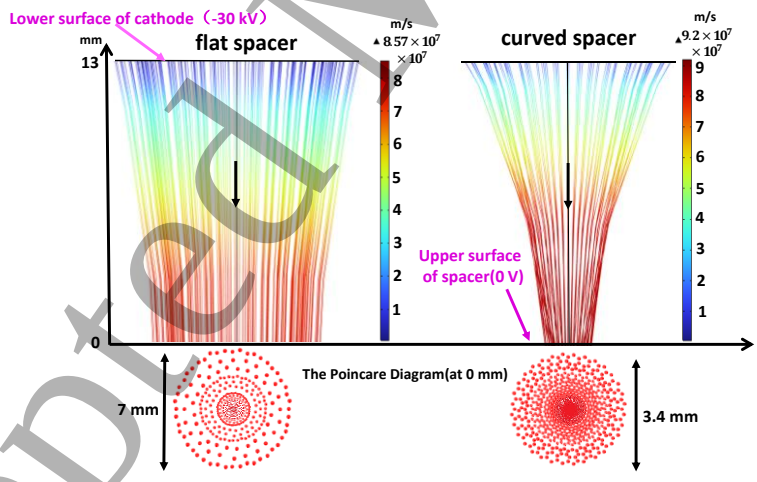

Figure 9. Comparison of particle trajectories under two types of spacer structures.

4 Experimental verification of the electron gun

4.1 Construction of the electron gun experimental platform

The experimental platform is shown in figure 10. To meet the requirements of electron gun ionization and lightweight design, the gun body is made entirely of aluminum, weighing 4 kg. The discharge chamber pressure is regulated through a feedback system, which involves a pressure control module and an intake proportional valve. During the electron gun beam experiments, a Faraday cup is placed in the lower vacuum chamber to receive the electron beam.

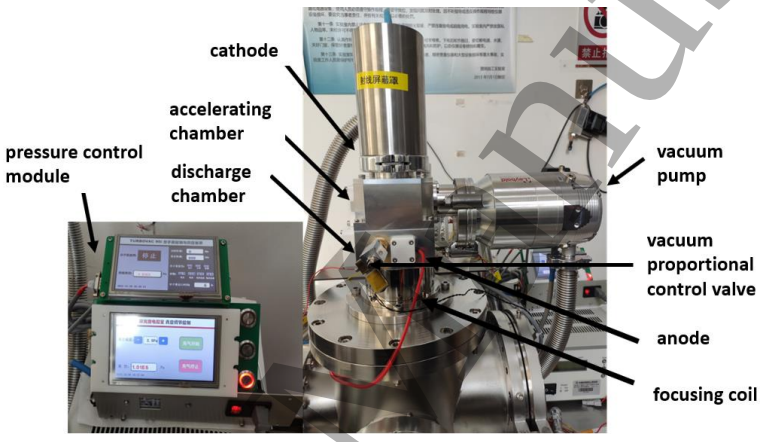

Figure 10. Electron gun experiment platform.

4.2 Experimental results of beam current under different pressures

In the experiment, the vacuum gauge and pressure regulation system were used to measure the pressure in the two chambers in real time. The discharge voltage was set at 1400 V, and the cathode voltage was adjusted to −27 kV, the electron gun beam current was measured under different discharge chamber pressures using the Faraday cup and the paperless recorder (MIK-R600C). The results are shown in figure 11. The experimental results indicate that when the discharge pressure is in the range of 5–8.5 Pa, the electron gun beam current is positively correlated with the plasma density in the discharge chamber. The formation of the electron beam is ultimately facilitated by the

increase in plasma density, which results in more ions being accelerated towards the cathode and leads to a higher yield of secondary electrons. The experimental results are consistent with the simulation results.

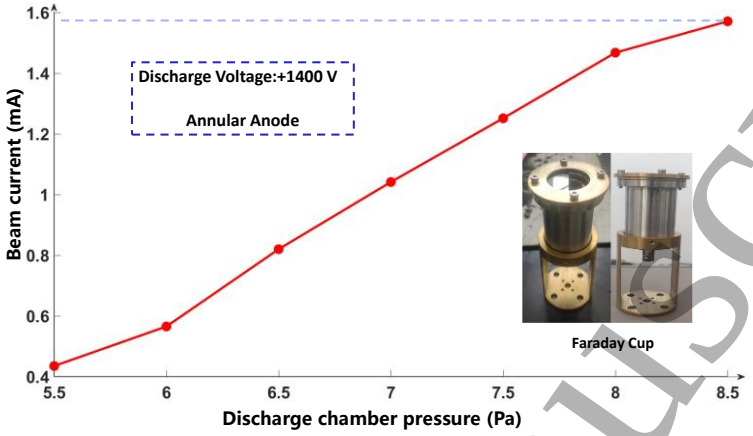

Figure 11. Comparison of beam current under different pressures.

When the discharge chamber pressure is further increased, although the plasma density in the discharge chamber is increased, the final beam current is decreased. This phenomenon is observed due to the pressure rises within the discharge chamber, which results in a corresponding rise in pressure within the accelerating chamber. Consequently, the ionization of the gas within the cathode-spacer gap is enhanced, with the density of charged particles and the conduction current through the cathode increased. The cathode is connected with a 100 kΩ resistor. When the voltage was 1400 V, the current in circuit of anode and ground was 10.84 mA (real-time measurement value from the high-voltage power supply), the anode voltage measured by the multi-meter was 316 V [25]. According to Ohm's law, as the conduction current in the circuit is increased, the negative high-voltage on the cathode block is decreased. This ultimately weakens the electric field between the cathode and the spacer gap. Consequently, secondary electrons are unable to acquire sufficient energy to

traverse the separator and form the electron beam. The beam current measurement results are shown in figure 12.

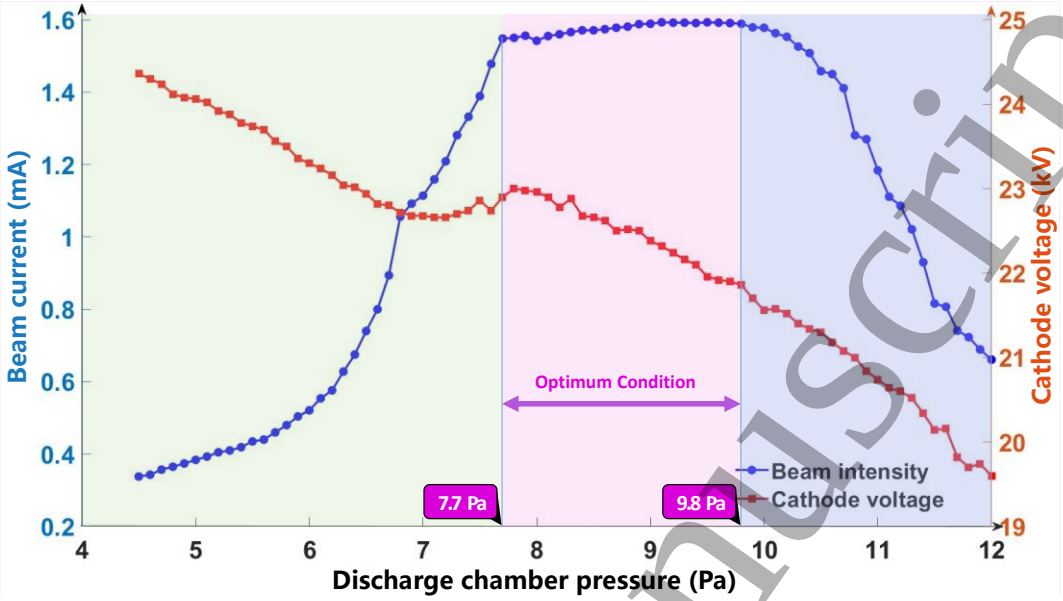

Figure 12. Comparison of beam current and cathode voltage results under different pressure.

In summary, there is a constrained relationship between the discharge chamber pressure and the final electron gun beam current, determined by factors such as the discharge circuit structure and the geometrical dimensions of the electron gun. When the discharge chamber pressure range is further expanded to 12 Pa, the beam current intensity will exhibit a maximum value near 7.7–9.8 Pa, and then the beam current will be decreased significantly. We define the range of discharge chamber pressures around this maximum value as the optimal pressure conditions for the SEEG.

4.3 Experimental results of beam current under different anode shapes

Using the optimized curved spacer, with the cathode at −30 kV and the anode at +1400 V remaining constant, the beam current measurements for two types of anodes under different discharge pressures are shown in figure 13.

The results indicate that at lower air pressure, i.e., lower plasma density, little diversity is shown in the plasma density between the two shapes of anode excitation, so that the difference in beam current intensity of the electron gun is not significant. However, as the pressure increases approaching the optimal pressure conditions, the difference in beam current intensity becomes more pronounced, and the shape of the anode determines the upper limit of the electron gun beam current. This is because the electrons are primarily originated from the large number of secondary electrons generated by ionic bombardment. Therefore, the upper limit of ion density near the central axis determines the upper limit of the electron gun beam current.

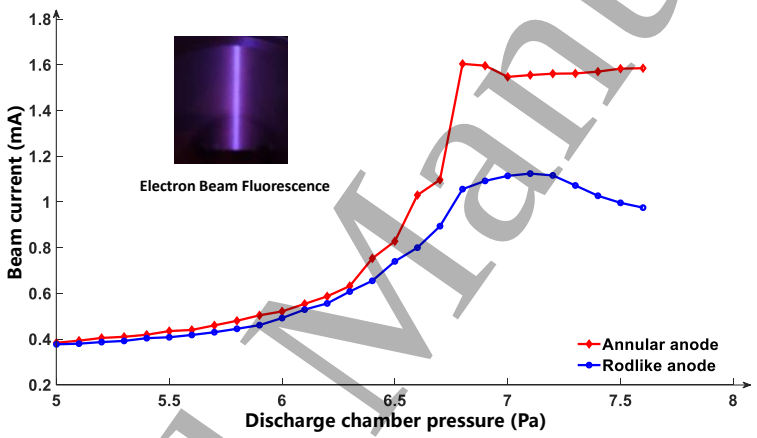

Figure 13. Comparison of the beam current with different anodes.

4.4 Experimental results of optimisation of the spacer structure

As shown in figure 14, when the voltage conditions remain unchanged, the beam current intensity of the SEEG under two different spacer structures is compared by varying the discharge chamber pressure. It can be observed that with the optimized spacer structure, the electron gun beam current can be increased by more than 77%, with the maximum beam current reached 1.6 mA. In summary, the anode shape, discharge pressure conditions, and the spacer structure can be optimized

to enhance the beam current of the ion bombardment SEEG effectively. The simulation and experimental measurement results are consistent.

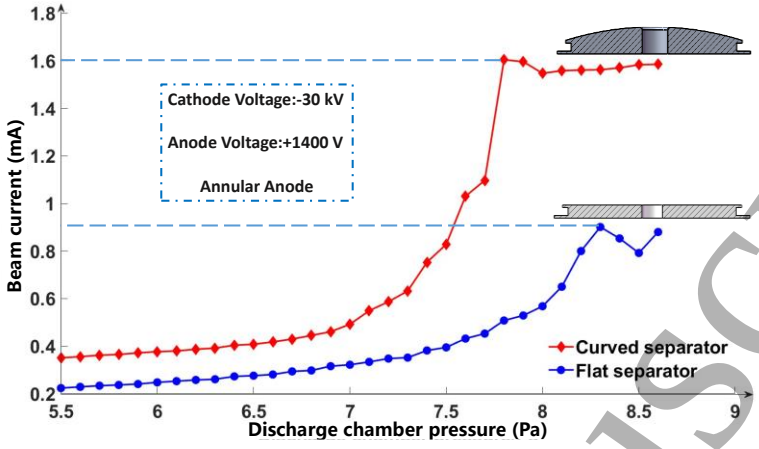

Figure 14. Comparison of electron gun beam current with different spacer structures.

5 Conclusion

To address the issue of small beam currents in existing ion bombardment SEEG structures, the limiting factors for the emission beam current of secondary emission electron guns under gas discharge theory are discussed. Through theoretical and structural analysis, it is determined that the primary reasons for the low electron beam current in existing designs stem from insufficient plasma density in the discharge chamber and a low transmission rate of secondary electrons through the spacer. Based on this analysis, two optimization directions are provided. First, the anode shape and discharge chamber pressure conditions are altered to improve the spatial distribution of plasma and increase ion density near the central axis of the discharge chamber, so that the issue of low secondary electron yield is resolved. Second, the spacer structure is optimized to improve the electric field distribution and gas resistance between the cathode and the spacer gap, thereby the cathode can withstand higher voltages and the transmission rate of secondary electrons can be increased through the aperture, thus the beam current can be better extracted. Additionally, comparative optimization simulation calculations are conducted using more realistic simulation models. The accuracy of the

simulation model and the feasibility of the two optimization methods for the beam current of SEEG are validated by the experimental results. Under conditions of 8.5 Pa discharge chamber pressure, −30 kV cathode voltage, and 1400 V anode voltage, the electron beam current of 1.6 mA can be obtained. In the future research, replacing the ion source for comparative experiments will be considered to further explore ways to increase the SEEG's beam current.

References

[1] Chen A G *et al* 2021 *Phys. Gases* **6** 67 (in Chinese)
[2] Choi Y M *et al* 2021 *Flow Meas. Instrum.* **82** 102074
[3] Nili-Ahmadabadi M *et al* 2021 *Eur. Phys. J. Plus.* **136** 953
[4] Estevadeordal J *et al* 2018 *Appl. Phys. B* **124** 41
[5] Chen A G *et al* 2024 *J. Exp. Fluid Mech.* **1** 8 (in Chinese)
[6] Diop B *et al* 2011 *Sensors* **11** 5202
[7] Lewis B M *et al* 2004 *IEEE Trans. Plasma Sci.* **32** 1242
[8] Whaley D R *et al* 2000 *IEEE Trans. Plasma Sci.* **28** 727
[9] Ustinovskii N N *et al* 1994 *Rev. Sci. Instrum.* **65** 2941
[10] Muntz E P 1968 *The electron beam fluorescence technique* Technical Editing and Reproduction Ltd., Paris, France
[11] Cherenshchikov S A *et al* 1955 *AIP Conf. Proc.* **337** 350
[12] Chalise P R *et al* 2004 *IEEE Trans. Plasma Sci.* **32** 1392
[13] Kui Z *et al* 2014 *Rev. Sci. Instrum.* **85** 093304
[14] Szapiro B and Rocca J J 1989 *J. Appl. Phys.* **65** 3713
[15] Michizono S 2007 *IEEE Trans. Dielectr. Electr. Insul.* **14** 583
[16] Wang D, He Y N and Cui W Z 2018 *J. Appl. Phys.* **124** 053301
[17] Feng Z H *et al* 2024 *Appl. Phys. Lett.* **125** 134101
[18] Huo W J *et al* 2024 *Plasma Sci. Technol.* **26** 055501
[19] Hagelaar G J M and Pitchford L C 2005 *Plasma Sources Sci. Technol.* **14** 722
[20] Zhao S X *et al* 2009 *J. Appl. Phys.* **105** 083306
[21] Korolev Y D *et al* 2022 *Plasma Sources Sci. Technol.* **31** 074002
[22] Boggasch E *et al* 1991 *Phys. Rev. Lett.* **66** 1705
[23] Salikeev S *et al* 2014 *Vacuum* **99** 303
[24] Qiu X L *et al* 2023 *Appl. Phys. Lett.* **122** 092902
[25] Fu W J *et al* 2010 *Appl. Phys. Lett.* **96** 071502